

# Finite-Difference Time-Domain (FDTD) Method with Non Homogeneous Cells Filled with Voxels

Kenan Tekbaş<sup>a,b</sup>, Jean-Pierre Bérenger<sup>c</sup>

<sup>a</sup> Department of Electrical and Electronic Engineering, Amasya University, Amasya 05100, Türkiye (currently on leave under MSCA grant at the University of Granada)

<sup>b</sup> Department of Electromagnetism and Matter Physics, University of Granada, Granada 18071, Spain

<sup>c</sup> Department of Electrical and Electronic Engineering, The University of Manchester, Manchester M139PL, U.K

**Abstract**— With the objective of reducing the overall number of FDTD cells in applications where the objects of interest are given as sets of voxels, as in bio-electromagnetism, a subcell technique is introduced to allow the FDTD method to account for non-homogeneous cells composed with voxels of different permittivity's. Numerical experiments with dielectric objects are reported to illustrate the effectiveness and the limitations of the method.

**Index Terms**—FDTD, subcell, voxel, multigrid.

## 1. Introduction

Several techniques were published in the past to enable the finite-difference time-domain (FDTD) method [1] to account for subcell structures. Dielectric, lossy, and dispersive sheets thinner than the cell size can be placed in the FDTD grid [2]-[7].

In this paper we show that the FDTD method can account for nonhomogeneous cells composed with voxels where each voxel has its own medium. As many others, the method relies on the application of the Maxwell-Ampère law in its integral form. It can be viewed as an extension of the thin sheet formalism [2], with which the subcell object is thinner than the cell size in the direction of the thickness, but assumed as of infinite extend in the other two directions. With the proposed formalism, the subcell structure can be of finite size in all the directions of space. It permits the FDTD cell to be split into voxels of any size while the Courant-Friedrich-Levy (CFL) stability condition of the FDTD scheme is left unchanged, i.e. it remains dependent on the cell size, not on the voxels size.

In the case of dielectric voxels, the proposed method can also be viewed as equivalent to the method [8] that allows staircased interfaces between media to be introduced in the FDTD cells. However, the proposed method is more general, since [8] relies on an effective permittivity in the cells where there are interfaces, so that it cannot be used with dispersive media where an auxiliary equation must be solved in each medium. This is also the case of the method [9, 10] which in addition is limited to a single plane interface in the cells. The methods [11, 12] can handle dispersive media but they are also limited to a single interface. From this, there is no method at hand in the literature to deal with FDTD cells filled with dispersive voxels, which is our objective. The method we developed, called the Voxel-In-Cell (VIC) method, inspired by what has been previously done with thin sheets [4, 5], permits our objective to be achieved.

The motivation of the introduction of the VIC method was not the inclusion of subcell structures, but rather the reduction of the computational burden in bio-electromagnetics where the objects are given as sets of voxels. This can be achieved by using VIC cells larger than the voxels. As an example, with a VIC cell two times larger than the voxels, i.e. with eight voxels in each VIC cell, the overall number of cells is reduced with a factor of eight, and the stability condition is relaxed with a factor of two, resulting in a large reduction of memory and CPU time requirements with respect with a calculation with a FDTD cell equal in size to that of the voxels.

The principle of the VIC method is presented in section 2, for simplicity in the case of dielectric media only. The case of dispersive Debye media where the relationship connecting  $E$  and  $D$  fields is dispersive, treated as in [4-5], will be the subject of a subsequent paper [13]. The objective of the present paper is mainly the evaluation of the loss of accuracy, when any, due to the use of VIC cells larger than the voxels, and the identification of the critical issues, if any, of the method. Various numerical experiments with dielectric objects are provided in two dimensions (2D) in section 4 and in three dimensions (3D) in section 5. They illustrate the possibilities and the limitations of the VIC method when used for the reduction of the computational burden. It is mainly shown that the VIC method does work with loss of accuracy limited to the proximity of singularities of the field [14]. Other potential applications of the VIC method are briefly addressed in the conclusion.

## 2. Theory of the Voxels in Cell Method

Let us consider a physical space split into voxels of sizes  $\delta x$ ,  $\delta y$ ,  $\delta z$ , where the media in the voxels may be different. We assume that a FDTD lattice is set in that space as in Fig. 1. Note the represented cell is the one that permits PEC or dielectric structures to be sets of cells, with  $E$  components on the edges of the cells and  $H$  components perpendicular to the faces. The ratios of the cell sizes  $\Delta x$ ,  $\Delta y$ ,  $\Delta z$  to the voxel sizes are integers  $M_i$ ,  $M_j$ ,  $M_k$ , that is  $\Delta x = M_i \delta x$ ,  $\Delta y = M_j \delta y$ ,  $\Delta z = M_k \delta z$ . We assume in the following that  $M_i$ ,  $M_j$ ,  $M_k$ , are even numbers.

To allow the  $E$  components to be updated at the nodes of the FDTD grid, we have to derive a scheme that can account for the nonhomogeneous medium composed with voxels inside the FDTD cells. Let us assume that the component to be updated is  $E_z$  at node  $(i_g, j_g, k_g)$  in Fig. 1. This component is redrawn in Fig. 2 at the center of a volume of sizes  $\Delta x$ ,  $\Delta y$ ,  $\Delta z$ , that is at the center of a FDTD cell shifted with  $\Delta x/2$  and  $\Delta y/2$  with respect with Fig.1. In the plane  $k = k_g$  that holds  $E_z$  there are nodes  $H_{y-}$  and  $H_{y+}$  situated  $\Delta x/2$  from  $E_z$ , and nodes  $H_{x-}$  and  $H_{x+}$  situated  $\Delta y/2$  from  $E_z$ . In the usual case where the medium and then the cells are homogeneous, these  $H$  components are used to update  $E_z$  by discretizing the integral form of the Maxwell-Ampere equation

$$\iint_{\Delta x \Delta y} \varepsilon \frac{\partial E_z(t)}{\partial t} dx dy = C_h(t) \quad (1)$$

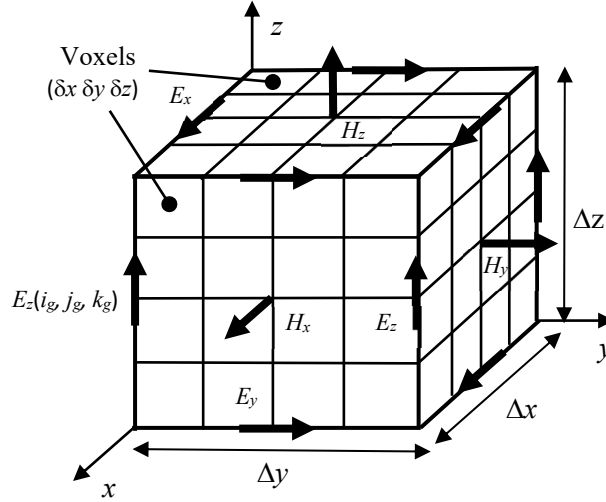


Fig. 1. One FDTD cell with voxels with different media in its interior.

where  $\varepsilon$  is the permittivity in the medium,  $t$  is the time,  $\Delta x \Delta y$  is the surface perpendicular to  $E_z$  at  $k = k_g$  and  $C_h$  is the integral

$$C_h(t) = \int_L H(t) dl \quad (2)$$

where  $L$  is the contour path that surrounds surface  $\Delta x \Delta y$  and holds the four  $H$  nodes. Discretizing the derivative on time in (1) yields the FDTD update in the homogeneous medium

$$E_z^{n+1}(i_g, j_g, k_g) = E_z^n(i_g, j_g, k_g) + \frac{\Delta t}{\varepsilon \Delta x \Delta y} C_h^{n+1/2} \quad (3)$$

usually rewritten as

$$E_z^{n+1}(i_g, j_g, k_g) = E_z^n(i_g, j_g, k_g) + \frac{\Delta t}{\varepsilon} \left[ \frac{H_{y+}^{n+1/2} - H_{y-}^{n+1/2}}{\Delta x} - \frac{H_{x+}^{n+1/2} - H_{x-}^{n+1/2}}{\Delta y} \right] \quad (4)$$

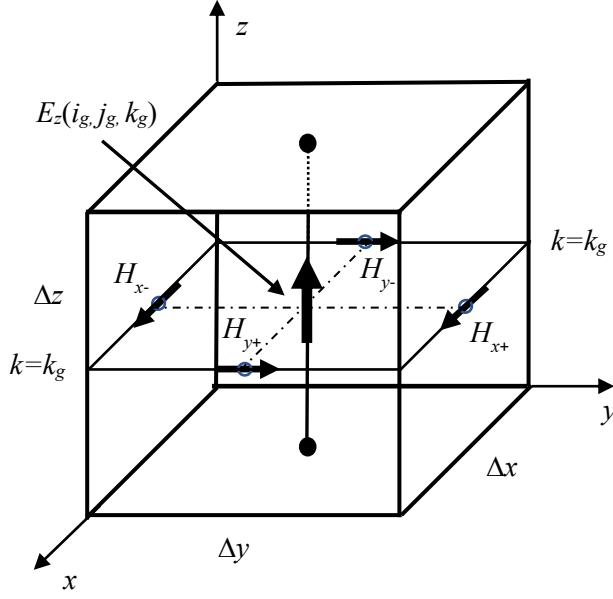


Fig. 2. FDTD cell  $\Delta x$ ,  $\Delta y$ ,  $\Delta z$  in size with component  $E_z$  at its center.

Let us now address the case where the cell in Fig. 2 is split into  $M_i M_j M_k$  voxels of indexes  $(i_v, j_v, k_v)$ , where  $i_v \in (1, \underline{M}_i)$ ,  $j_v \in (1, \underline{M}_j)$ ,  $k_v \in (1, \underline{M}_k)$ . Each voxel has its own medium. The FDTD cell can be viewed as composed with  $M_k$  slices, each one being  $\delta z$  in thickness and composed with  $M_i M_j$  voxels. Slice  $k_v=2$  is represented in Fig. 3. Component  $E_z$  is parallel to the interfaces between the voxels of each slice and thus continuous through these interfaces. Since with FDTD the cell is small with respect with the wavelength,  $E_z$  can thus be assumed as uniform in each slice, i.e. it is the same in all the voxels of a considered slice. Conversely,  $E_z$  is not continuous at the interfaces between slices, because it is perpendicular to these interfaces. We have thus one unknown  $E_z(k_v)$  to be updated in slice  $k_v$ , that is  $M_k$  unknowns  $E_z(k_v)$  to be updated in the FDTD cell centered at node  $E_z(i_g, j_g, k_g)$ .

The Maxwell-Ampere law (1) holds everywhere in the physical medium, in particular in the slices composed with voxels. Assuming that  $C_h$  is a constant over the cell, from  $z = z(k_g) - \Delta z/2$  to  $z = z(k_g) + \Delta z/2$ , which is consistent with the homogeneity of the permeability  $\mu$  in the cell, we can do what is done with homogeneous cells to derive the FDTD equation of the update of  $E_z$  in each slice, with no more assumption on the Physics. For slice  $k_v$ , (1) yields the discrete integral at time  $t$

$$\sum_{i_v=1}^{M_i} \sum_{j_v=1}^{M_j} \varepsilon(i_v, j_v, k_v) \frac{\partial E_z(k_v, t)}{\partial t} \delta x \delta y = C_h(t) \quad (5)$$

Discretizing the derivative on time yields

$$E_z^{n+1}(k_v) = E_z^n(k_v) + \frac{\Delta t}{\varepsilon^*(k_v)} \left[ \frac{H_{y+}^{n+\frac{1}{2}} - H_{y-}^{n+\frac{1}{2}}}{\Delta x} - \frac{H_{x+}^{n+\frac{1}{2}} - H_{x-}^{n+\frac{1}{2}}}{\Delta y} \right] \quad (6)$$

where

$$\varepsilon^*(k_v) = \frac{\sum_{i_v=1}^{M_i} \sum_{j_v=1}^{M_j} \varepsilon(i_v, j_v, k_v)}{M_i M_j} \quad (7)$$

is the average value of the permittivity in slice  $k_v$  of the cell centered at node  $E_z(i_g, j_g, k_g)$ .

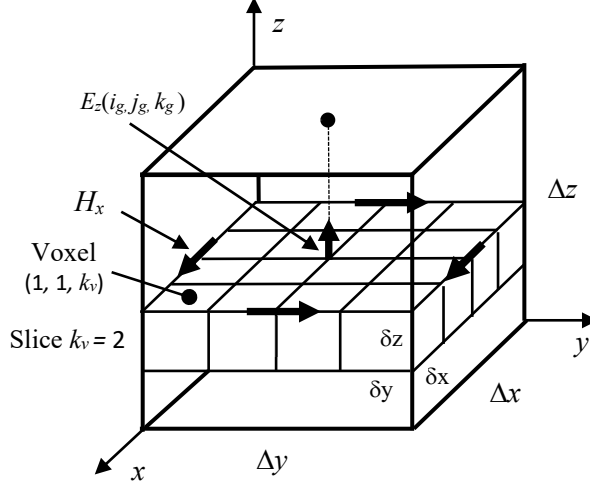


**Fig. 3.** Non homogeneous FDTD cell composed with voxels of size  $\delta x \delta y \delta z$  filled with different media. The  $M_k$  slices considered to derive the update of  $E_z$  component are composed with  $M_i M_j$  voxels and are perpendicular to the  $z$  direction. One slice ( $k_v=2$ ) is represented in the figure.

Once  $E_z(k_v)$  and its  $x$  and  $y$  counterparts have been updated in all the slices of all the FDTD cells, the  $H$  components should be updated to complete the FDTD iteration. Applying the Maxwell-Faraday law in integral form, updating  $H$  at the four neighboring nodes represented in Fig. 2 requires the integral of  $E_z$  over the segment  $\Delta z$  that holds the  $E_z(i_g, j_g, k_g)$  node. With non-homogeneous cells,  $E_z$  depends on the slice. Computing the integral is trivial. In practice, since the integral is nothing but the average of  $E_z$  over  $\Delta z$  multiplied with  $\Delta z$ , and since the permeability is homogeneous in the cells, the standard FDTD algorithm of the update of the  $H$  components can be left unchanged, one has just to put the average value  $\langle E_z^{n+1} \rangle$  at every original  $E_z(i_g, j_g, k_g)$  node of the FDTD cells, that is

$$E_z^{n+1}(i_g, j_g, k_g) = \frac{1}{M_k} \sum_{k_v=1}^{M_k} E_z^{n+1}(k_v) \quad (8)$$

Finally, with cells filled with voxels, the FDTD update of the  $E$  components can be summarized as follows

1. Compute  $E_z^{n+1}(k_v)$  in each slice of the cell centered at  $E_z(i_g, j_g, k_g)$  using (6),
2. Compute the average of  $E_z^{n+1}(k_v)$  in the cell using (8), to be used later for the update of  $H$  components,
3. Proceed similarly for the  $E_x$  and  $E_y$  components.

We note that the bracket in (6) is the same for the  $M_k$  slices, so that steps 1 and 2 can be merged and  $E_z^{n+1}(i_g, j_g, k_g)$  computed as follows, without explicit computation of the  $M_k E_z^{n+1}(k_v)$ , which may be of interest for saving memory and CPU time:

$$E_z^{n+1}(i_g, j_g, k_g) = E_z^n(i_g, j_g, k_g) + \frac{\Delta t}{\varepsilon^{**}(i_g, j_g, k_g)} \left[ \frac{H_{y+}^{n+\frac{1}{2}} - H_{y-}^{n+\frac{1}{2}}}{\Delta x} - \frac{H_{x+}^{n+\frac{1}{2}} - H_{x-}^{n+\frac{1}{2}}}{\Delta y} \right] \quad (9)$$

where

$$\frac{1}{\varepsilon^{**}(i_g, j_g, k_g)} = \frac{1}{M_k} \sum_{k_v=1}^{M_k} \frac{1}{\varepsilon^*(k_v)} \quad (10)$$

Comparing (10) with [equ. (6), 8], the VIC method is equivalent to [8], with both methods the FDTD scheme can be left unchanged using permittivity (10) with VIC or the effective permittivity in [8]. But this is only true with dielectric media. In the case of dispersive media, the  $E$  field should be explicitly computed in the VIC slices [13].

Concerning the update of the  $H$  components, since the permeability is uniform in the cell it is the same as with the usual FDTD scheme, using the updated VIC  $E$  components (8) or (9).

Since both the  $E$  components (8) or (9) and the  $H$  components are computed at the same nodes as in the normal cells of the FDTD grid, part of a computational domain can be normal cells, i.e. cells in vacuum or in any other medium, and the other part can be cells with voxels inside, as in the computational domain depicted in Fig. 4. There is no need of particular conditions at the interfaces between the two parts.

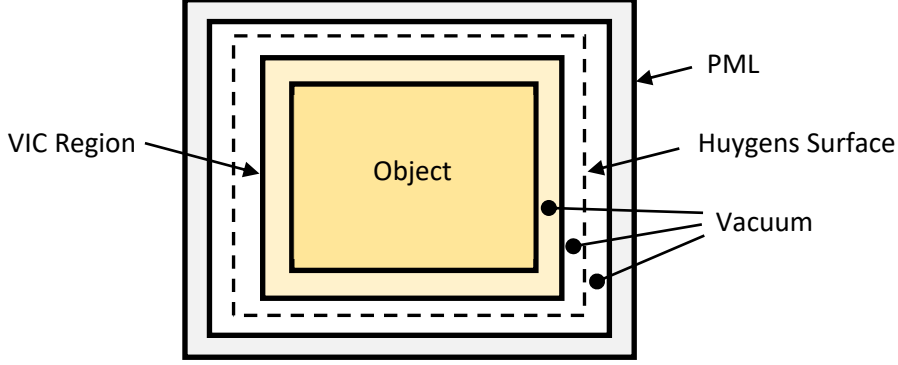


**Fig. 4.** The computational domain used in the 2D and 3D numerical experiments. The VIC region is a few cells larger than the object with voxels filled with vacuum in the VIC cells outside the object. In the interface between the VIC region and the outer FDTD grid, the standard FDTD equations of vacuum can be used to update the two  $E$  components.

### 3. The Methods with which VIC is compared in the Numerical Experiments

In the next sections, VIC calculations are compared to the other two following calculations:

1/ a reference calculation with a FDTD fine grid whose cell is superimposed to the voxels and has the same sizes  $\delta x$ ,  $\delta y$ ,  $\delta z$ . The  $E$  nodes are located on the edges of the fine cells. The permittivity used to update an  $E$  component is consistent with the Maxwell-Ampere law, in 3D it equals the average of the permittivity's in the four surrounding voxels, in 2D it equals the average of the permittivity's in the two pixels contiguous to the  $E$  node.

2/ a calculation, denoted as AVG in the following, with a coarse grid whose FDTD cell has same sizes  $\Delta x$ ,  $\Delta y$ ,  $\Delta z$  and same location as the VIC cell (Fig. 1). As with the Dey-Mitra technique [15], the permittivity used to update  $E$  equals the average permittivity in the volume  $\Delta x$ ,  $\Delta y$ ,  $\Delta z$  whose center is the considered  $E$  node. In 3D, this reads, for component  $E_z(i_g, j_g, k_g)$

$$\varepsilon(i_g, j_g, k_g) = \frac{\sum_{i_v=1}^{M_i} \sum_{j_v=1}^{M_j} \sum_{k_v=1}^{M_k} \varepsilon(i_v, j_v, k_v)}{M_i M_j M_k} \quad (11)$$

We note that inserting (7) into (10) results in  $\varepsilon^{**}$  that differs from  $\varepsilon$  (11), because (10) is the average of the inverses of  $\varepsilon^*$ , instead of the average of  $\varepsilon^*$  in (11). The VIC permittivity (10) accounts for the discontinuity of  $E$  perpendicular to the interfaces between slices, average value (11) does not. The difference between the VIC and AVG methods is like the difference between Luebbers [3] and Maloney [2] methods for thin sheets, one takes account of the discontinuity, the other does not.

### 4. Two dimensional numerical experiments

In the following, 2D experiments are reported for canonical problems where the field reduces to  $E_x$ ,  $E_y$ ,  $H_z$  components. The corresponding 2D VIC mesh is represented in Fig. 5 in the case where the ratio of the VIC cell to the voxels size equals 2, i.e.  $M = \Delta x/\delta x = \Delta y/\delta y = 2$ .

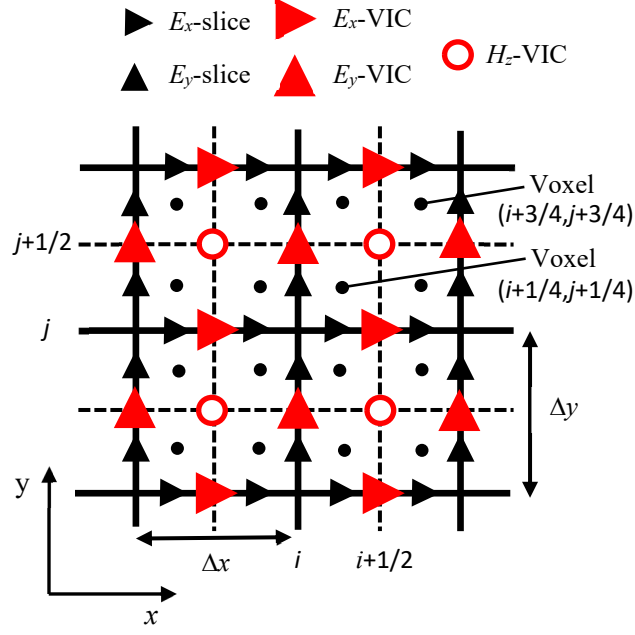


**Fig. 5.** The 2D VIC mesh with four voxels in each VIC cell ( $\Delta x/\delta x = \Delta y/\delta y = 2$ ). The nodes of the VIC components denoted as  $E_x$ -VIC,  $E_y$ -VIC,  $H_z$ -VIC are situated as in the normal FDTD mesh.  $E_x$ -VIC,  $E_y$ -VIC are updated with the 2D counterpart of (8).  $E_x$ -slice and  $E_y$ -slice denote  $E_x$  and  $E_y$  in the slices, updated with the 2D counterpart of (6). Their nodes are situated  $\Delta x/4$  and  $\Delta y/4$  from  $E_x$ -VIC and  $E_y$ -VIC nodes, respectively.

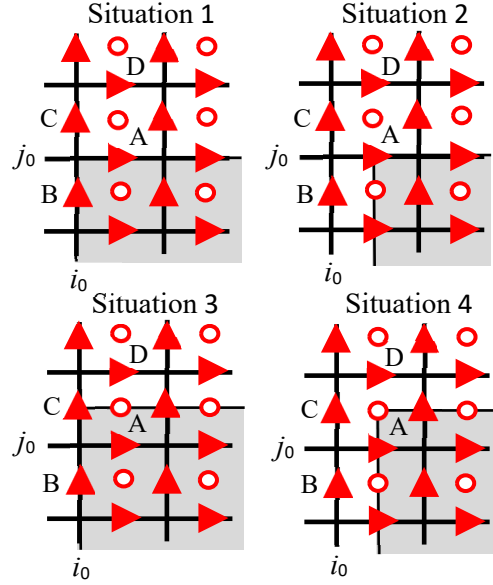


**Fig. 6.** The four situations of the upper left corner of the 20x20 square in the VIC grid. The grey part is the square where  $\epsilon_r = 50$ , with  $\epsilon_r = 1$  in the surrounding vacuum. The  $E$  field at  $E_x$ -VIC node A, and at  $E_y$ -VIC nodes B and C, are plotted in Figs. 7-9.  $E_x$ -VIC at node D node is used in Fig. 13.

In the experiments, the VIC-cell sizes were  $\Delta x = \Delta y = 2$  mm with time step  $\Delta t = 4.48$  ps (1 mm and 2.24 ps in the fine grid). A square of size 20x20 VIC cells, i.e. 40x40 voxels, of permittivity  $\epsilon_r = 50$ , was placed in a vacuum ( $\epsilon_r = 1$ ). With ratio 2, there are four possible situations of the square with respect with the VIC grid, i.e. four situations of the upper-left corner of the square, as represented in Fig. 6. With situation 1, the corner is at location  $(i_0, j_0)$  in the grid, with situation 2 it is at  $(i_0+1/2, j_0)$ , with situation 3 at  $(i_0, j_0+1/2)$ , and with situation 4 at  $(i_0+1/2, j_0+1/2)$ . One may expect that the computed results will depend on the location of the corner, at least in its close vicinity.

The FDTD domain (Fig. 4) was composed with a central part of 30x30 VIC cells placed within a normal FDTD grid with the same space step as that of the VIC part (2 mm). The square with  $\epsilon_r = 50$  was placed in the 20x20 central part of the VIC grid, with  $\epsilon_r = 1$  outside it in the VIC grid. An incident plane wave propagating in  $x$  direction

was radiated by a Huygens surface set in the normal FDTD grid (Fig. 4). Its waveform was

$$E_y(t) = 100 \exp[-((t - 3\tau)/\tau)^2] \text{ V/m} \quad (12)$$

where  $\tau = 134.5$  ps, which allows the wavelength at 10 % of the peak value (3.7 GHz) to be about 40 and 6 space steps in the vacuum and in the dielectric.

According to the theory in section 2,  $E_x$ -slices and  $E_y$ -slices were computed at their nodes using (6). These nodes are represented in Fig. 5 (black nodes), but are omitted in Fig. 6. And from (8), the VIC  $E_x$  and  $E_y$  (red nodes in Figs. 5 and 6) were computed as the averages of two  $E_x$ -slices or two  $E_y$ -slices. Obviously, the VIC  $E_x$  and  $E_y$  could also be obtained in a direct manner using (9).

Figs. 7-9 report  $E_x$  at VIC node A and  $E_y$  at VIC nodes B and C, all situated in the close vicinity of the corner (Fig. 6). The left parts of Figs. 7-9 compare the VIC solution with the fine grid solution, for the four situations of the corner (Fig. 6). Similarly, the right parts compare the AVG solution with the fine grid solution. Note that the  $E$  nodes of the VIC and AVG grids are not collocated with fine grid nodes, they are located at mid distance from two fine grid nodes. From this, for the comparisons in the figures, we use the average value of  $E$  at these two fine grid nodes.

For  $E_x$  at location A (left part, Fig. 7), the VIC results are close to the fine grid reference results in situations 1, 2, and 3. VIC and fine grid peak values only significantly differ, by about 15%, in situation 4 (red curves). Inversely, AVG strongly differs from fine grid in situations 2 and 4 (right part, Fig. 7, red and blue curves). Note that in situation 1 the VIC and AVG curves are identical. This is because the permittivity's of the two  $E$ -slices (7) at any VIC node equal the AVG permittivity (13). From this, VIC and AVG fields are identical at any node of the grid.

For  $E_y$  at B and C nodes (Figs. 8 and 9), the largest error of VIC is again in situation 4 while AVG solutions are strongly erroneous in situations 2 and 4 at B, and in situations 2 and 3 at C.

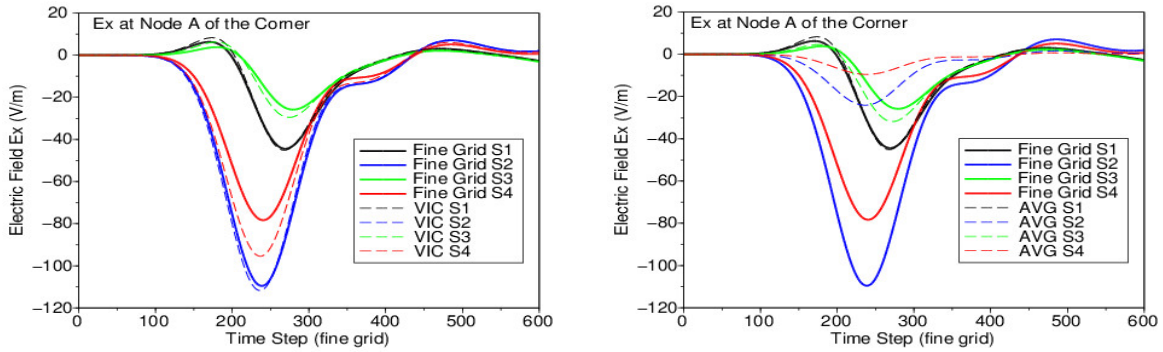


**Fig. 7.** Results at the corner. Comparison of  $E_x$  in fine grid with  $E_x$  at node A computed either with VIC (left part) or AVG (right part), for situations S1, S2, S3, and S4 of the corner (Fig. 6). S1 and S3 results (black and green curves) are multiplied with 5 to render the differences more visible.

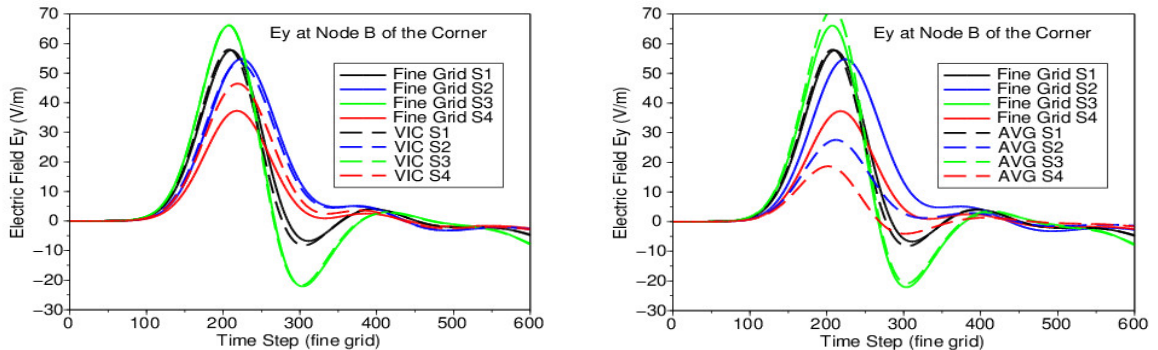


**Fig. 8.** Results at the corner. Comparison of  $E_y$  in fine grid with  $E_y$  at node B computed either with VIC (left part) or AVG (right part), for the corner situations S1, S2, S3, and S4. S1 and S3 curves are multiplied with 5.

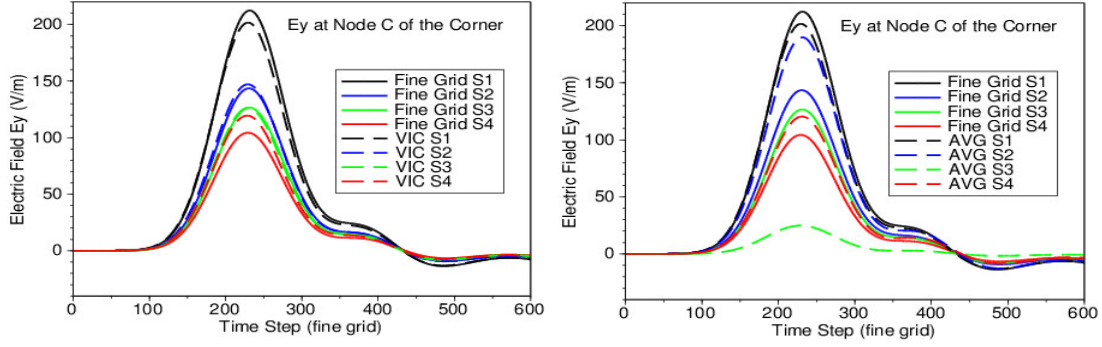


**Fig. 9.** Results at the corner. Comparison of  $E_y$  in fine grid with  $E_y$  at node C computed either with VIC (left part) or AVG (right part), for the corner situations S1, S2, S3, and S4.

In summary to the results reported in Figs. 7-9 and to others not reported here, in three situations of the corner with respect with the VIC grid, VIC yields  $E$  field that is close to the fine grid solution in the vicinity of the corner and on the interface. In the fourth situation, the VIC results differ from the fine grid results with 10-15 %. As a whole, VIC is a large improvement with respect with the averaging method (AVG) with which the  $E$  field differs from the fine grid reference with a factor that may be of the order of 4 or 5 in some cases. Other experiments were performed with other incidence angles  $\theta$  with respect with  $x$  direction ( $\theta = 0$  in Figs. 7-9). The difference between VIC and fine grid weakly depends on the incidence  $\theta$ , the smallest difference was observed with  $\theta = 45^\circ$ .

Other results computed with the  $20 \times 20$  square are provided in Figs 11-12. The  $E$  field is plotted at nodes F, G, P, and Q, depicted in Fig. 10. Nodes F and G are about the interface between vacuum and the square of  $\epsilon_r = 50$ , they are roughly 3 VIC cells from the corner. Nodes P and Q are in the vacuum, roughly 3 VIC cells from the square.

Fig. 11 (left part) shows  $E_x$  at F node, for situations 1, 2, 4 of the corner. Node F is upon the interface in situations 2 and 4 while it is inside the dielectric in situation 1. In the three situations the VIC  $E_x$  agrees very well with the fine grid, inversely to the AVG  $E_x$  that differs from the fine grid  $E_x$  with a factor of the order of 10 in situations 2 and 4. This is because in situations 2 and 4 the two  $E_x$ -slices of VIC at F node are updated with the exact permittivity's of the two media, while the AVG  $E_x$  is updated with their average value, so that VIC can account for the discontinuity of  $E$  normal to the interface, AVG cannot. For  $E_y$  at G node (Fig. 11, right part) which is also either on the interface or  $\Delta x/2$  from it, VIC is almost perfect. The AVG error is small, about 10 % only in situation 4, because  $E_y$  is parallel to the interface and thus continuous. In summary to the experiments in Fig. 11, and to others not reported, at nodes in the vicinity of interfaces and far from corners, VIC provides us with results almost superimposed on the fine grid reference, even with such high contrasts as 50 between the permittivity's of the two media.

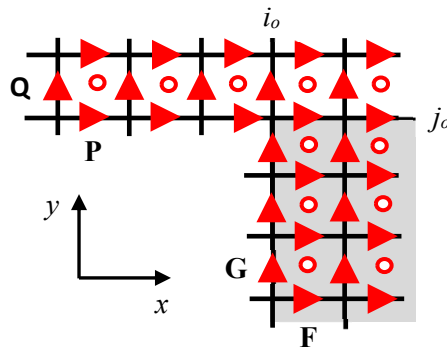


**Fig. 10.** Outputted nodes in the vicinity of the interface (nodes F and G) and far from the corner of the square (nodes P and Q). The square is represented in situation 1.

Figs. 12 show  $E_x$  and  $E_y$  away (3 cells) from any interface or corner, in the homogeneous vacuum. As can be observed, VIC and fine grid results are superimposed, while a small difference is visible between AVG and fine grid results. In fact, in a homogeneous medium, permittivity  $\epsilon_r$  is the same in fine grid, VIC, and AVG calculations. No difference is produced locally, at nodes P and Q in Fig. 10. Nevertheless, the results are not superimposed, rigorously, because the spurious field produced by VIC (at corner) and AVG (at corner and interface) are different, the one of AVG is larger, it is thus visible at P and Q nodes, while the one of VIC is not.

The conclusion of the experiments in Fig. 12, and of others we performed, is that even in the homogeneous parts of the computational domain close to interfaces or corners, VIC is better than AVG, because VIC produces no discrepancy at interfaces and a smaller discrepancy at corners.

As a conclusion to the 2D experiments with cells two times larger than the voxels, the VIC calculations yield accurate results at most nodes of the computational domain. This is only at nodes close to the 2D corners where a significant difference between fine grid reference and VIC is observed. This suggests that the observed difference is due to the singularity of the  $E$  field near the corners [14]. This was expected since increasing the size of the FDTD cell always results in a poorer sampling of the singular  $E$  fields. This is confirmed in the next section with 3D experiments.

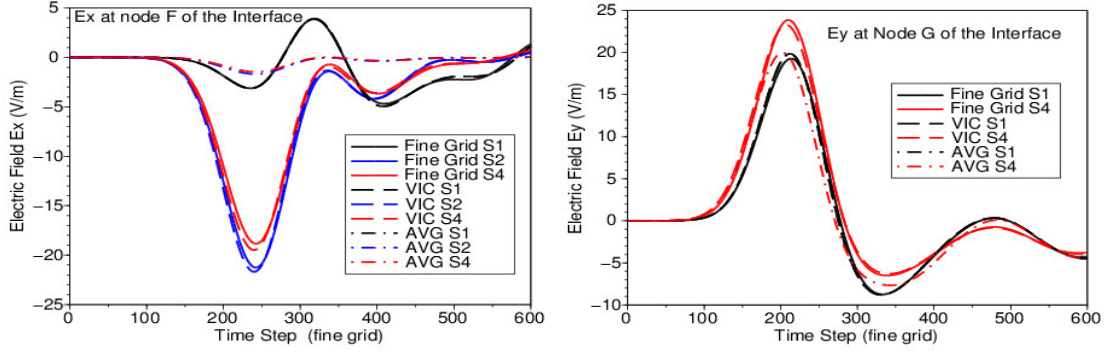


**Fig. 11.** Results in the vicinity and on the interface, some distance from the corner. Comparison of  $E_x$  in fine grid with  $E_x$  at F node (left part) and G node (right part), computed either with VIC or AVG. At F node the plotted situations are S1, S2, and S4, with S1 curves multiplied with 5. At G node the plotted situations are S1 and S4. Note that at F node, AVG results in situations S2 and S4, almost superimposed in the figure, are strongly erroneous.

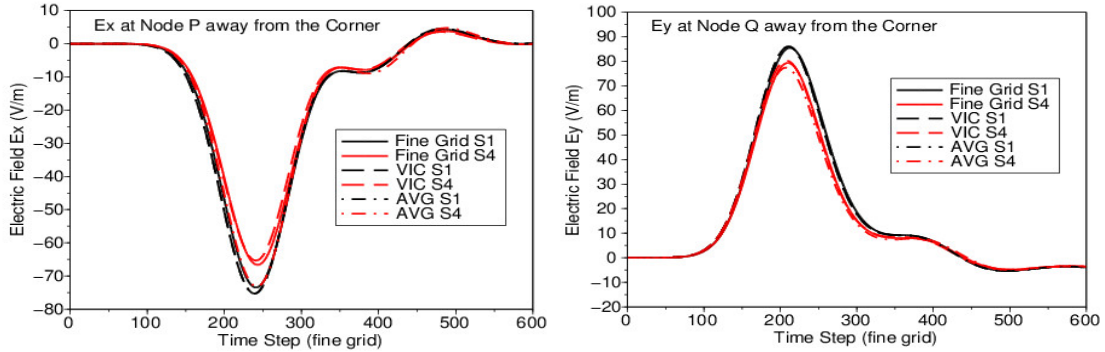


**Fig. 12.** Results far from the corner and the interface. Comparisons of  $E_x$  at P node (left part) and  $E_y$  at Q node (right part) computed in fine grid with  $E_x$  and  $E_y$  computed either with VIC or AVG, for the corner situations S1 and S4.

Other 2D experiments were performed with VIC cells four times larger than the voxels, that is  $M_i = M_j = 4$ . Figs. 13 and 14 report results for a 20x20-VIC-cell square composed with 80x80 voxels. There are 16 possible situations of the square in the VIC grid. One situation is the same as situation 1 in Fig. 6, with 16 voxels in each VIC cell instead of 4.  $E_x$  and  $E_y$  were outputted at four nodes located as A, B, C, D in Fig. 6, for all the 16 situations. The VIC cell was 4 mm in size and the width of the incident pulse was two times larger than in (12).

As with the ratio of grids equal to 2 in Figs. 7-9, VIC agrees well with the fine grid calculations in most situations. In some, the disagreement is larger than the one observed in Fig. 7 in situation 4, which seems consistent with a larger ratio of grids. In Figs. 13 and 14 we report synthetic comparisons of VIC with AVG. The differences between VIC and fine grid fields at A, B, C, D were added over the 16 situations at every time step  $it$ , and normalized to the sum of the peak values of the 16 fine grid  $E$  fields. As an example, for  $E_x$  at node A, this reads

$$DE_{xVIC}(A, it) = \frac{\sum_{m=1}^{16} |E_{xVIC}(A, it, m) - E_{xfine}(A, it, m)|}{\sum_{m=1}^{16} |E_{xfine-peak}(A, m)|} \quad (13)$$

where  $m$  is the situation of the square in the VIC grid. Similar differences were computed with the AVG results. Figs. 13 and 14 compare the VIC differences with the AVG differences. This can be viewed as comparisons of the

average VIC error with the average AVG error for the set of 16 situations. One can see that the VIC calculations are not perfect, but the VIC error measured by the above formula is widely smaller than that of the AVG, by a factor of 3-5.

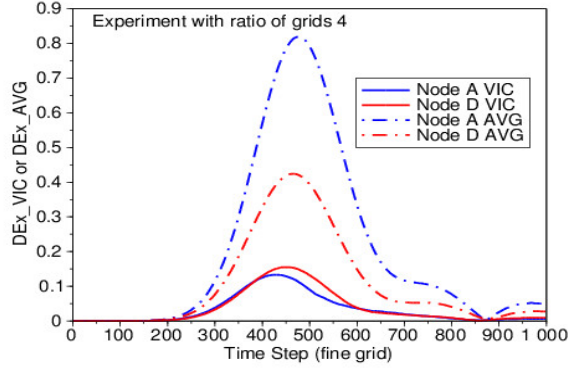


**Fig. 13.** A 20x20-VIC-cell square with ratio of VIC cell size to voxels size  $M_i = M_j = 4$ . Difference of  $E_x$  between VIC or AVG and fine grid at nodes A and D in Fig. 6. The plotted curves are the addition of the differences of the 16 situations of the square as in (13).

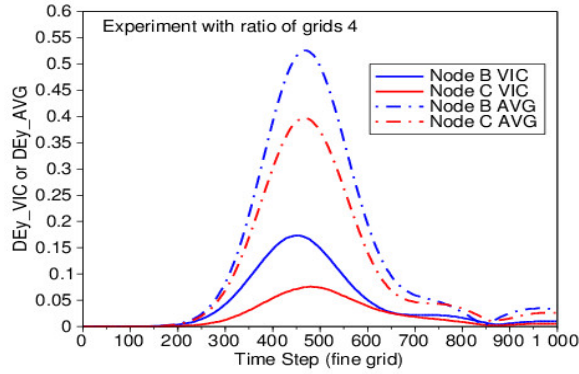


**Fig. 14.** A 20x20-VIC-cell square with ratio of VIC cell size to voxels size  $M_i = M_j = 4$ . Difference of  $E_y$  between VIC or AVG and fine grid at nodes B and C in Fig. 6. The plotted curves are the addition of the differences of the 16 situations of the square as in (13).

## 5. Three dimensional numerical experiments

In this section, results of 3D experiments are reported in the case where the ratio of the VIC cells size to the voxels size equals 2. The VIC cell, with eight voxels inside, is depicted in Fig. 15. As in 2D, two  $E$ -slice nodes (in black) are associated with each  $E$ -VIC node (in red), and the  $E$ -VIC and  $H$ -VIC nodes are located as in a usual FDTD cell. Again, this implies that no particular conditions are needed at an interface between a normal FDTD grid and a VIC grid.

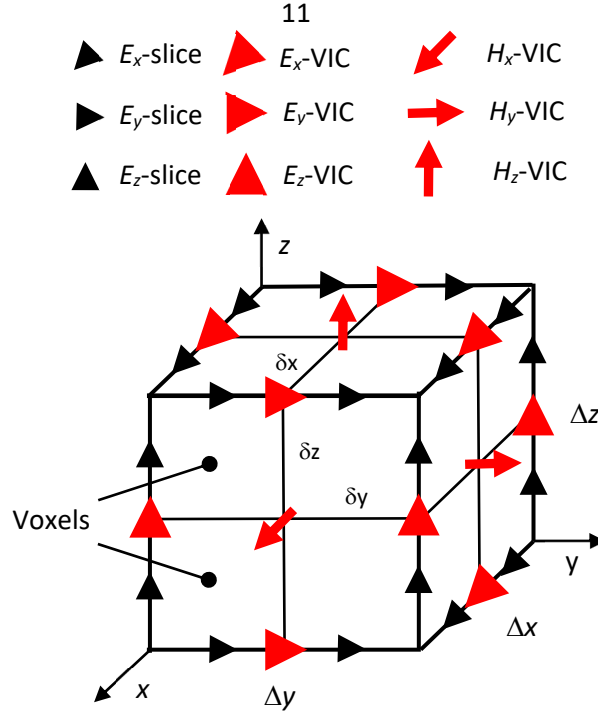


Fig. 15. The VIC cell composed with 8 voxels, with the locations of the  $E$ -slice,  $E$ -VIC, and  $H$ -VIC nodes.

The FDTD update of each  $E$ -slice component is performed with (6). Then the  $E$ -VIC components are updated using (8). With the possibility of merging the two steps using (9).

Since in 2D an amount of inaccuracy was observed nearby corners, the 3D experiments were mainly focused on the corners and edges where the  $E$  field is singular (sub-sections 5.1 and 5.2). Especially, at dielectric edges [14], the transverse components of  $E$  behave as

$$E_t(r) = \frac{A v}{r^{1-v}} [\cos v(\varphi + \alpha)u_r - \sin v(\varphi + \alpha)u_\varphi] \quad (14)$$

where  $r$  is the distance from the edge and the other parameters are given in [14]. Parameter  $v$  is smaller than unity so that  $E_t(r)$  tends to infinity as  $r$  vanishes. Note this formula does not depend on frequency, it is valid as long as  $r$  is much less than the wavelength. The 3D experiments we performed with edges, as the one reported in sub-section 5.2, clearly confirmed that near an edge the  $E$  component parallel to the edge is accurately computed by VIC, while the two transverse components may suffer from inaccuracy. Moreover, the Fourier transforms of the VIC results show that the inaccuracy, when any, as in the results in sub-section 5.3, does not depend on frequency, in accordance with (14). At 3D corners where all the components are singular, all may be inaccurate in some situations of the corner, and again the inaccuracy does not depend on frequency. All this proves that the inaccuracy of VIC, more precisely the difference between VIC and fine grid calculations, is due to the sharp variation of the singular  $E$  fields at some locations, near edges and corners of objects. Such a drawback is always present with the FDTD method, even the fine grid calculations are not perfectly accurate at singular locations. With VIC the step size is at least doubled, with the consequence that the inaccuracy is larger.

Concerning the  $H$  field in the VIC grid, since  $H$  is never singular with homogeneous permeability [14] it was expected that  $H$  will be accurate in the whole VIC domain. This has been confirmed by many experiments, not reported in this paper. The VIC  $H$  field is almost superimposed to the fine grid  $H$  field at any node, the error is quite small, similar to the error of the  $E$  field far from singularities.

In addition to the experiments with pure canonical structures, we performed experiments with a 60x60x60-VIC-cell cube composed with three media of relative permittivity's of 50, 30, and 5. Although by far simpler, this object resembles to a Human Body, the permittivity's are of the order of those of Human tissues, 50 is close to that of Skin, and 5 is close to that of Fat. A more realistic model of tissues is the Debye medium, but even in that case the dielectric constant is the preponderant physical parameter. From this, the object permits evaluation of the accuracy of VIC in view of its extension to Debye media and applications to bioelectromagnetics. The results of the experiments are reported in sub-section 5.4. They show that the difference between VIC results and fine grid results is rather smaller than with the pure canonical objects, mainly because the contrast of permittivity between media at singular locations is lower.

### 5.1 Experiments with a corner of a cube

The object was a dielectric ( $\epsilon_r = 50$ ) cube of  $40 \times 40 \times 40$  VIC cells placed in vacuum. The FDTD steps were  $\Delta x = \Delta y = \Delta z = 1$  mm and  $\Delta t = 1.83$  ps for the fine mesh and  $\Delta x = \Delta y = \Delta z = 2$  mm and  $\Delta t = 3.66$  ps for the VIC mesh. The incident plane wave was the same Gaussian pulse as in 2D (12). The incident plane wave had the same Gaussian pulse shape as in 2D (12) and was propagating in  $y$  direction, with the  $E$  field polarized in  $z$  direction. We outputted the  $E$  field in the vicinity of a corner, at the nodes shown in Fig. 16. With ratio of grids 2, there are 8 possible situations of the corner with respect with the VIC grid.

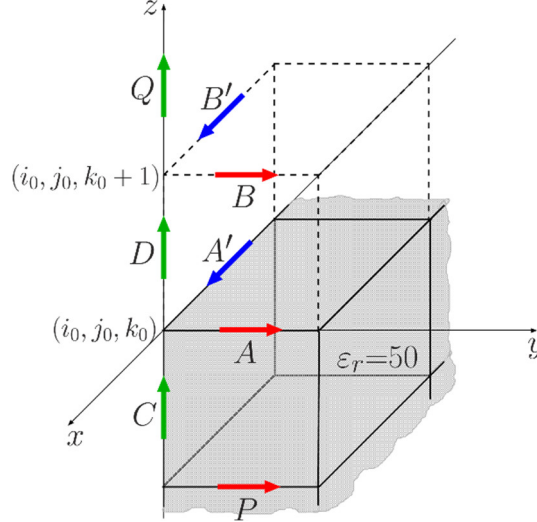


**Fig. 16.** The corner in the VIC grid with 8 possible situations. Situation 1 with the corner at  $(i_0, j_0, k_0)$ , situation 2 at  $(i_0 - 1/2, j_0, k_0)$ , situation 3 at  $(i_0, j_0 + 1/2, k_0)$ , situation 4 at  $(i_0 - 1/2, j_0 + 1/2, k_0)$ , situation 5 at  $(i_0, j_0, k_0 + 1/2)$ , situation 6 at  $(i_0 - 1/2, j_0, k_0 + 1/2)$ , situation 7 at  $(i_0, j_0 + 1/2, k_0 + 1/2)$ , situation 8 at  $(i_0 - 1/2, j_0 + 1/2, k_0 + 1/2)$ .

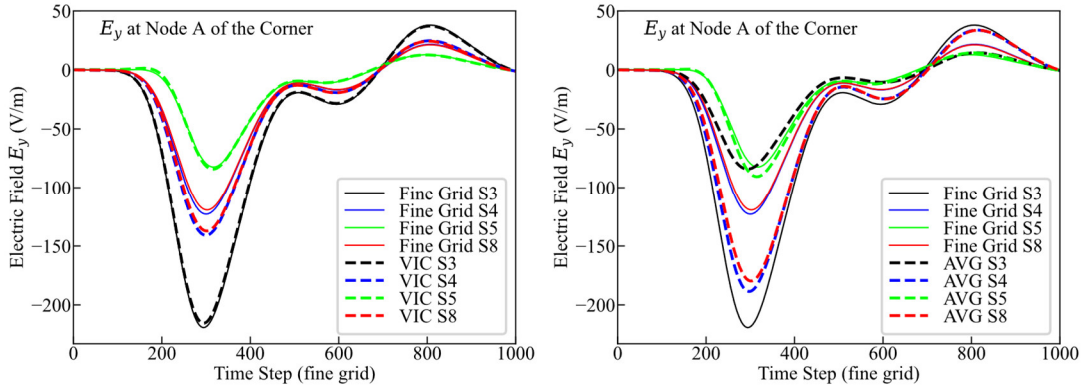


**Fig. 17.** Results at the corner. Comparison of  $E_y$  in fine grid with  $E_y$  at  $A$  node computed either with VIC (left part) or AVG (right part), for the corner best two (S3 and S5) and worst two (S4 and S8) situations of the corner. S5 results (green curves) are multiplied with 5.

Figs. 17-19 compare the VIC and AVG  $E$  fields with the reference fine grid fields, at  $A$ ,  $C$ , and  $D$  nodes. Each figure shows the best two situations of the corner, i.e. the ones that yield the smallest two VIC inaccuracies in the peak values, and the worst two situations, i.e. the ones that yield the largest two VIC inaccuracies. It can be seen that the VIC accuracy widely depends on the situation of the corner. In the best situations the VIC field is about superimposed on the fine grid solution, while in the worst situations the error is typically of the order of 10-20% in the peak value.

Concerning the AVG inaccuracy, it is quite large in some situations. As an example, at node  $A$  in situation 3, VIC is almost perfect (black curves in Fig. 17), while AVG is about three times smaller than the fine grid solution. This can be easily understood using Fig. 16. In situation 3 the corner is shifted by half a cell to the right, it is at  $A$ . From this, the AVG permittivity at  $A$ , i.e. the average of those of the 8 surrounding voxels (11) is  $57/8 = 7.125$ . Inversely, with VIC, one  $E$ -slice is in vacuum, while the other is surrounded with 3 voxels of vacuum and one voxel of dielectric. The permittivity's used to updated the two  $E_x$ -slices (7) are thus 1 and  $53/4 = 13.25$ , respectively. From this, the integral of  $E_x$  (8) used to update  $E_x$ -VIC accounts for the physical discontinuity of  $E_x$  at  $A$ . VIC accounts for Physics, AVG does not. A similar problem occurs at  $D$  in situation 5, with also an AVG error by a factor about 3.

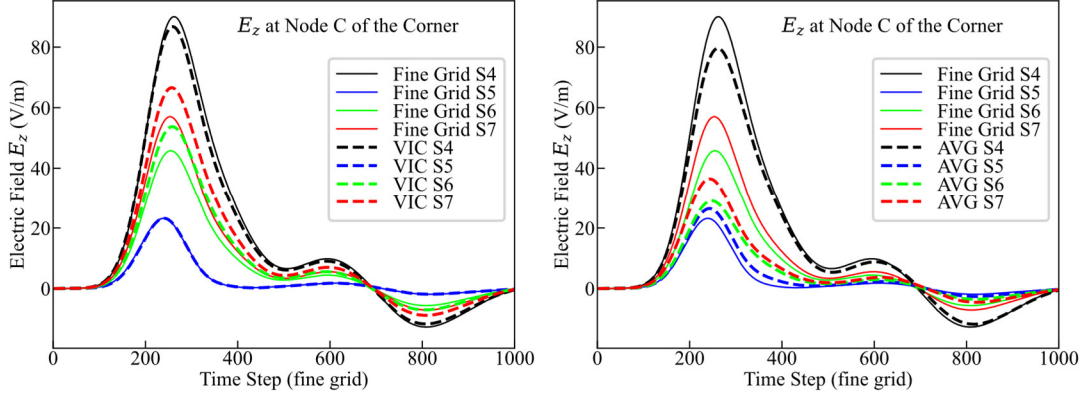


**Fig. 18.** Results at the corner. Comparison of  $E_z$  in fine grid with  $E_z$  at C node computed either with VIC (left part) or AVG (right part), for the corner best two (S4 and S5) and worst two situations (S6 and S7) of VIC. S6 results (green curves) are multiplied with 0.8.

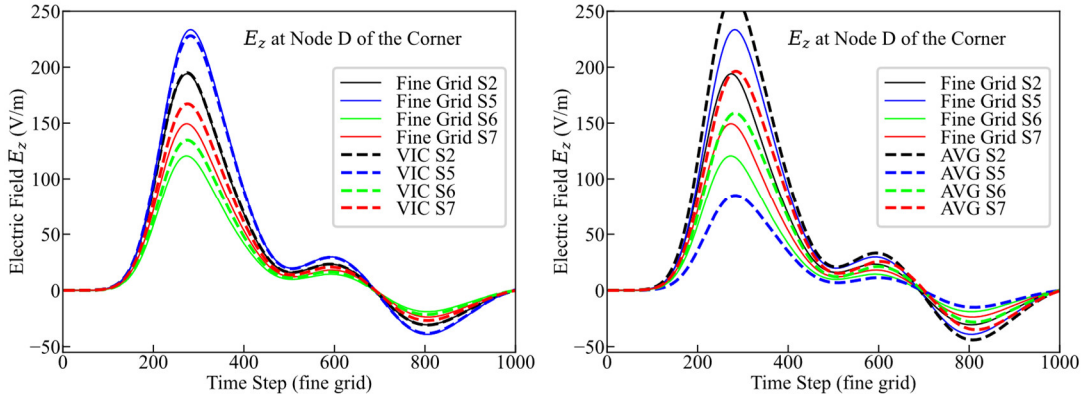


**Fig. 19.** Results at the corner. Comparison of  $E_z$  in fine grid with  $E_z$  at D node computed either with VIC (left part) or AVG (right part), for the corner best two (S2 and S5) and worst two (S6 and S7) situations of VIC. For the purpose of illustrating the large AVG errors when the corner is at a VIC node, as at D in situation S5, one of the best two situations, S3, is replaced with S5 with which the VIC error is close to that of S3. S6 results (green curves) are multiplied with 0.8.

At the nodes where the corresponding  $E$ -slice nodes are in the same media, as at A in situations 4 or 8, the AVG permittivity is correct, equal to that of the two VIC slices, but errors come from other nodes where it is not correct, so that at all the nodes nearby the corner the AVG error is always larger than the VIC one, as observed in Figs. 17-19.

Beside time domain results in Figs. 17-19, Figs. 20 and 21 provide with a synthetic information on the inaccuracy, mainly in the form of the errors of VIC and AVG methods on their peak values, at all the nodes in Fig. 16 and for all the 8 situations of the corner. More precisely, for a given node and a given situation, the VIC and AVG bars in Figs. 20 or 21 were computed as

$$Err = \frac{|E_{peak}(VIC \text{ or } AVG) - E_{peak}(fine)|}{|E_{peak}(fine)|} \quad (15)$$

where  $E_{peak}(VIC \text{ or } AVG)$  and  $E_{peak}(fine)$  are the peak values of VIC or AVG, and of fine grid calculations. In Fig. 20 the incident wave is the same as in Figs. 17-19, while in Fig. 21 its propagation forms the angles  $30^\circ$  with  $+y$  axis and  $60^\circ$  with  $-z$  axis, while the incident  $E$  remains in the  $(y, z)$  plane. We clearly observe that, as a whole, in both figures the VIC error is by far smaller than the AVG error. Additional results are provided in Figs 20 and 21, in the inserts that show the errors at A, B, C and D nodes, in function of time, calculated using a formula like (13), where the errors at each node are averaged over the 8 situations. Again, as a whole, the VIC error (continuous lines) is by far smaller than the AVG error (dashed lines).

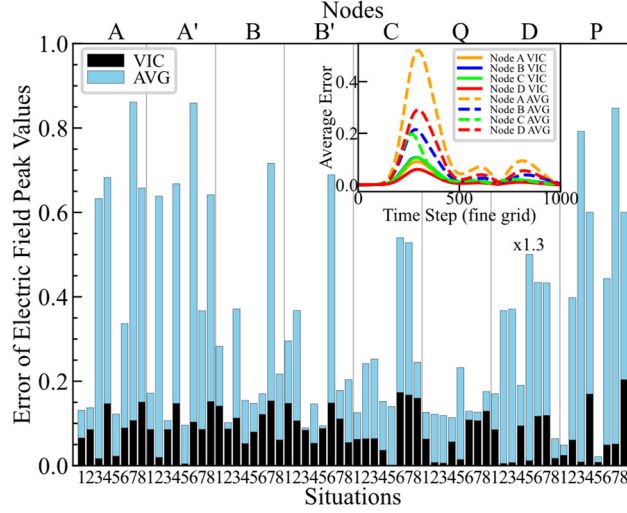


**Fig. 20.** Peak-to-peak error (15) for VIC and AVG calculations at all the nodes in Fig. 16 and for the 8 situations of the corner. The S5 bars of node D were downscaled 1.3 in height.

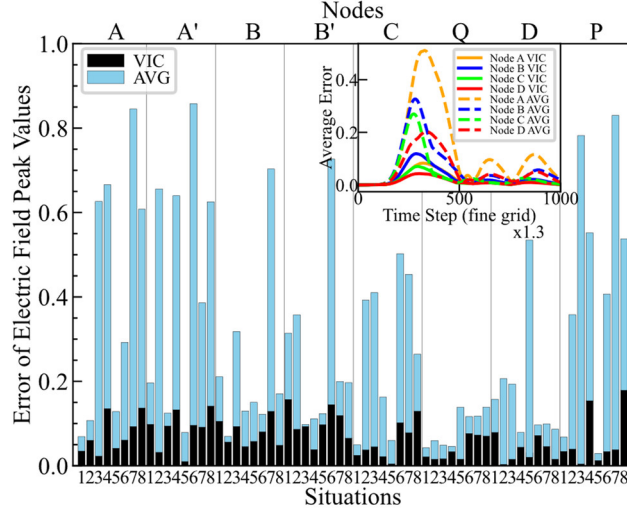


**Fig. 21.** Peak-to-peak errors (15) for VIC and AVG with an oblique incident wave.

## 5.2 Experiments with an edge of a cube

From the edge point of view, i.e. if the edge were infinite in  $z$  direction (Fig. 16), the sets of four situations of the object S1-S4 and S5-S8 are undistinguishable. Thus, there are only 4 different situations of the edge, the one in Fig. 22 and the others shifted with  $1/2$  in  $i$  or  $j$ , or both, as at a 2D corner. However, the VIC errors produced by the corners situated at finite distances can propagate to the location of the observation on the edge. To render this corner error negligible at the observation nodes, the cube in Fig.16 was enlarged in  $z$  direction to 100 VIC cells and the  $E$  field was observed in the vicinity of the point  $(i_o, j_o, k_o)$  located 20 VIC cells below the top corner of the cube. The results of situations S1-S4 and S5-S8 remained slightly different for physical reason, since the distances of the corners differ with  $1/2$  cell, but not for numerical reason.

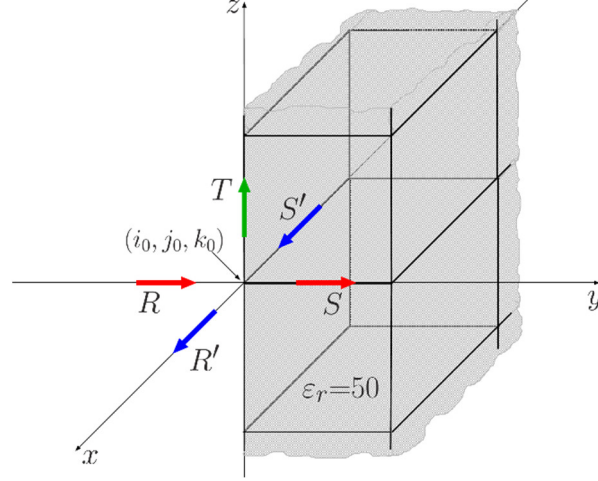


**Fig. 22.** The edge in the VIC grid with 4 possible situations. The edge pierces the plane  $k = k_0$  at  $(i_0, j_0, k_0)$  in situation 1, at  $(i_0 - 1/2, j_0, k_0)$  in situation 2, at  $(i_0, j_0 + 1/2, k_0)$  in situation 3, and at  $(i_0 - 1/2, j_0 + 1/2, k_0)$  in situation 4. The  $E$  field (Fig. 23) was observed at five nodes, it is normal to the edge at S, S', R and R', and parallel to the edge at T.

Fig. 23 shows the  $E$  field at the 5 nodes in Fig. 22, for two different incident waves, and in the situation 4 with which the observed VIC errors are the largest for the set of situations S1-S4. In both figures a significant VIC error is present on the  $E$  components perpendicular to the edge, at nodes R, R', S, S'. Inversely, the VIC  $E$  field at node T is superimposed to its fine grid counterpart, i.e. the component parallel to the edge is accurately computed by the VIC scheme. In situations 1, 2, and 3, not reported here, the observations are similar, an amount of VIC error is present in some cases at R, R', S, S', while in all the situations the  $E$  parallel to the edge at T is accurately computed. This confirms that the VIC inaccuracy is due to the singularity of some components of the  $E$  field, since at a dielectric edge [14] the transverse components are singular while the parallel component is not.

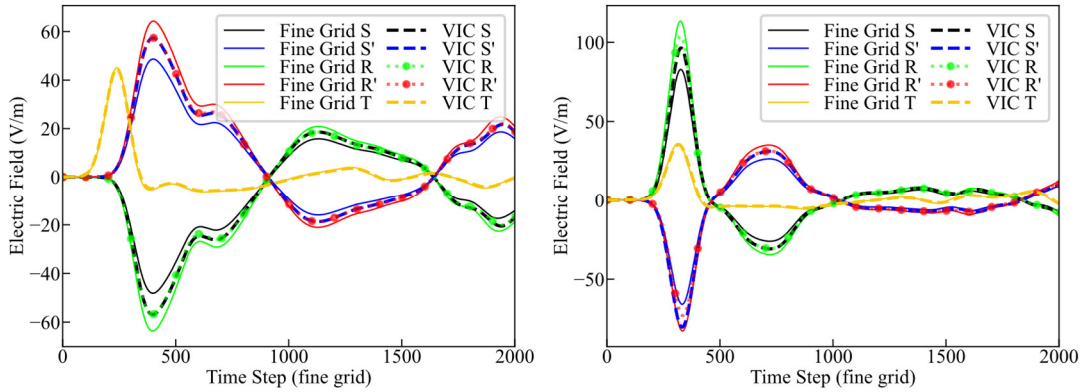


**Fig. 23.** Results at the edge with situation 4. In the left part, the propagation of the incident wave is the same as in Figs. 17-19. In the right part, the incident wave forms the angles  $45^\circ$  with  $+y$  and  $-z$  axes, while the incident  $E$  is lying in the  $(y, z)$  plane.

### 5.3 Frequency domain results

We performed some VIC and fine grid calculations up to 10 000 fine grid time steps. Note that no instability was observed with such long lasting VIC calculations. We then performed Fourier transforms of the results and applied the Hamming apodization function

$$A(t) = [0.54 + 0.46 \cos(\pi t/t_{max})] \quad (16)$$

An example of results is provided in Fig. 24 that is the frequency domain counterpart of the time domain Fig. 23 (left part), more precisely the Fourier transforms of the  $E$  fields at R, S, T nodes. We can see that the relative errors in Fig. 24 do not depend on frequency, at least at low frequency, for wavelengths large v.s. the space step. This agrees with the Van Bladel formula (14) of edges, and is another confirmation that the VIC errors are mainly due to the singularities. It is consistent with the fact that the relative errors are approximately constant over the time, as in Fig. 23 and in Figs. 17-19 of the corner. We can also see that the relative errors at S and R nodes are the same in time domain (Fig. 23, left part) as in frequency domain (Fig. 24), which is also consistent with the independence of the errors with frequency.

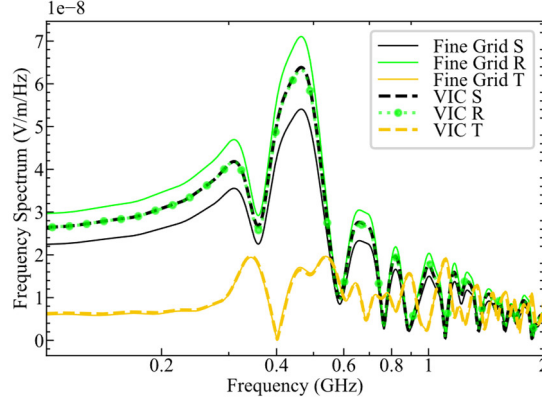


**Fig. 24.** Fourier transforms of  $E$  field at S, R and T nodes of the edge in situation 4. The spectra of S' and R' are almost superimposed to the ones of R and S, respectively.

Results similar to those in Fig. 24 were observed at other nodes near the corner or the edge, with the same conclusions, i.e. the VIC errors are due to singularities.

#### 5.4 An experiment with a Complex Object

We applied the VIC method to a  $60 \times 60 \times 60$ -VIC-cell cube composed with three media (Fig. 25) mimicking the topology of the Human Body. The object has a skin ( $\epsilon_r = 50$ ) with thickness 5 VIC cells. The size of the inner part ( $\epsilon_r = 30$ ) is  $30 \times 30 \times 50$  VIC cells, it is surrounded by a layer of thickness 10 VIC cells ( $\epsilon_r = 5$ ). We placed the object into vacuum and located some observation nodes at inner and outer corners, edges and interfaces. The incident wave is the same as in Figs. 17-19.

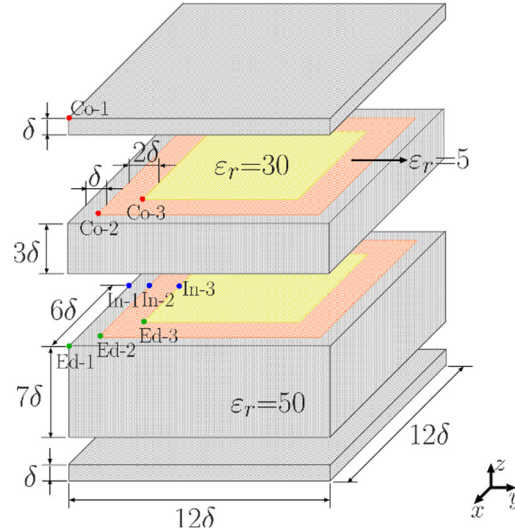


**Fig. 25.** The object mimicking the Human Body with three media of relative permittivity's of 50, 30, and 5.  $\delta = 5$  VIC cells. Points denoted as Co-, Ed-, and In-, are locations of corners, edges, interfaces, where  $E$  fields are plotted in Figs. 26-29.

As with any other object, there are 8 different situations of the object in Fig. 25 with respect with the VIC grid. The situations of corners Co-1, Co-2, and Co-3 are the same S1-S8 as those of the corner of the homogeneous cube in Fig. 16. For the edges, the observation locations Ed-1, Ed-2, and Ed-3, are at least 15 VIC cells from corners so that the VIC error that comes from corners is negligible. From this, and as with the edge in sub-section 5.2, the results computed with sets S1-S4 and S5-S8 are close to each other. We consider set S1-S4 in the following. Concerning the interfaces In-1, In-2, In-3, perpendicular to  $y$ , it can be seen that if they were infinite in  $x$  and  $z$  directions, sets of situations (S1, S3), (S2, S4), (S5, S7), and (S6, S8), would be indistinguishable, there would be only 2 different situations that would differ with a shift of  $1/2$  VIC cell in  $y$ . With the observation locations at least 20 cells from corners and edges as in Fig. 25, the results computed with the four sets are close to each other. We consider the set (S1, S3) in the following.

Figs. 26 and 27 show  $E_y$  and  $E_z$  at nodes A and C of the inner corners Co-2 and Co-3. The locations of A and C

with respect with points Co-2 or Co-3 in Fig. 25 are the same as those of A and C with respect with  $(i_o, j_o, k_o)$  of the corner in Fig. 16. The results at the outer corner Co-1, not reported here, are quite similar to those of the homogeneous cube in Figs. 17 and 18. It can be observed that the worst two VIC errors at inner corners Co-2 and Co-3 are much smaller than the ones at the outer corner of the homogeneous cube (Figs. 17 and 18). This was expected, since the contrast of the permittivity's at the inner corners is lower, 50/5 and 30/5, instead of 50/1.

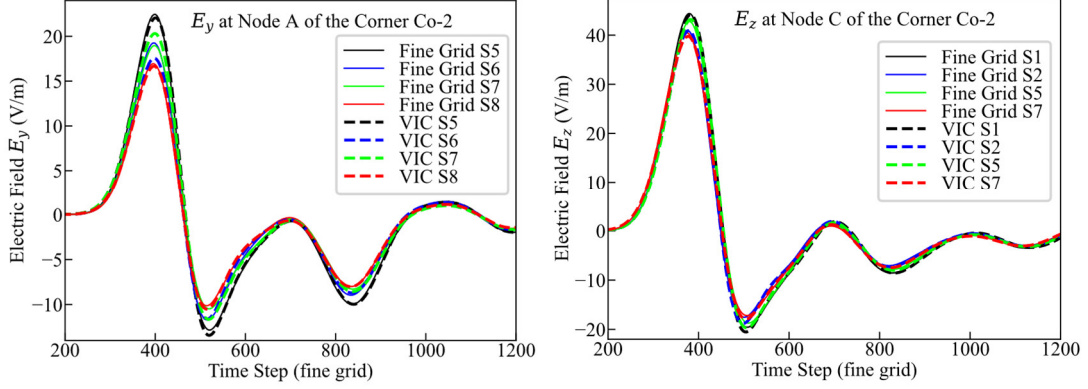


**Fig. 26.** Results at the inner corner Co-2. Comparison of fine grid  $E$  with VIC  $E$  at node A (left part) and at node C (right part). The best and worst two situations of VIC at node A are (S5 and S8) and (S6 and S7), respectively. The errors at node C are so small in all the situations that any situation can be considered as almost exact.

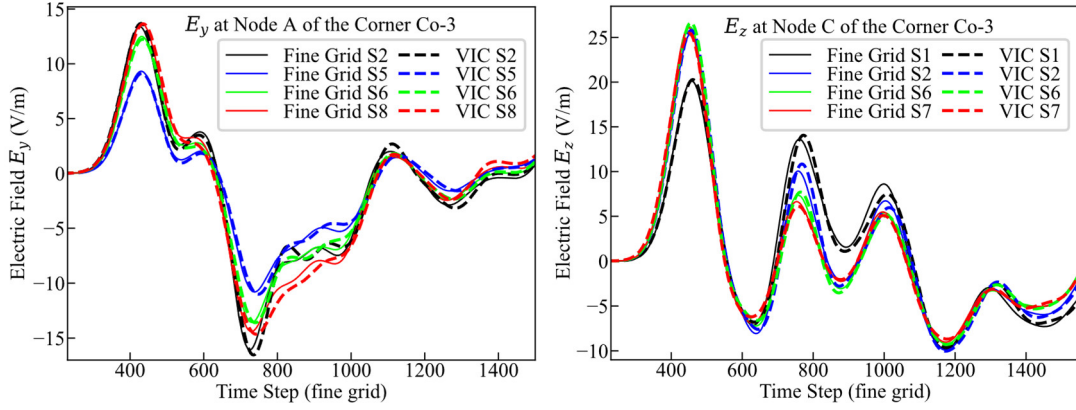


**Fig. 27.** Results at the inner corner Co-3. Comparison of fine grid  $E$  with VIC  $E$  at node A (left part) and at node C (right part). The best and worst two situations of VIC at node A are (S5 and S6) and (S2 and S8) whereas, at node C, they are (S6 and S7) and (S1 and S2) respectively.

The  $E$  components at the inner edges Ed-2 and Ed-3 are plotted in Fig. 28 at nodes R, R', S, S', and T, situated as in Fig. 22 with respect with the edges, and in situation 4 that produces the worst results at R, R', S, S' nodes where  $E$  is normal to the edges. Although we observe some errors at these nodes, the errors are smaller than the ones in Fig. 23, due to the smaller contrast of the permittivity's. Concerning  $E$  at T, which is parallel to the edge, as in Fig. 23 it is accurately computed, which again confirms that the VIC error at some nodes is due to the singularity of the  $E$  field.

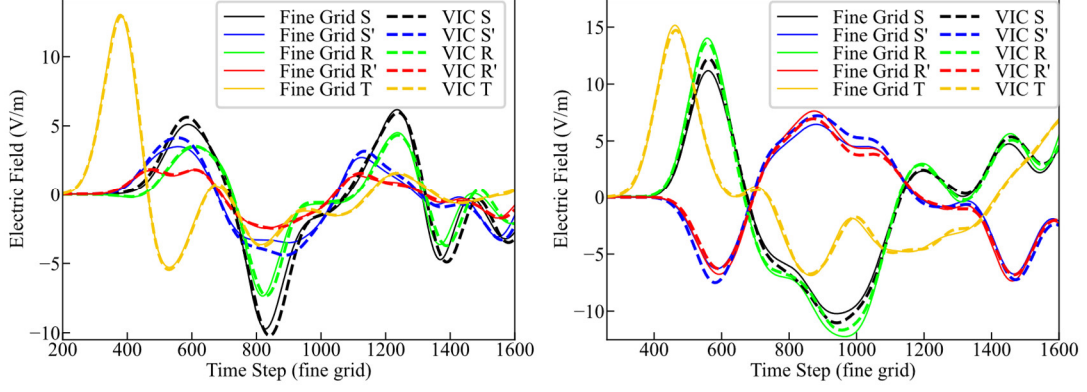


**Fig. 28.** Results with situation 4 at edge Ed-2 (left part), where node T results are multiplied with 0.25, and with situation 4 at edge Ed-3 (right part), where node T results are multiplied with 0.5.

Fig. 29 shows  $E_y$  field at interfaces In-1 and In-3, for the situations S1 and S3. With S1 the  $E_y$  node is 1/2 cell from the interface, in the interior of the media  $\epsilon_r = 50$  at In-1 or  $\epsilon_r = 30$  at In-3. With S3 it is on the interfaces. In both situations the VIC  $E_y$  is in perfect agreement with the fine grid  $E_y$ . Inversely, the AVG  $E_y$  is strongly erroneous in situation S3. This is because with S3 the two  $E_y$ -slices of the VIC node are updated with the exact epsilon's of the two media, that are different (1 and 50 for In-1, 5 and 30 for In-3), while the AVG  $E_y$  is updated with their average value (25.5, 17.5). Again, as in 2D, VIC can accurately account for the discontinuity of the  $E$  field normal to interfaces, regardless of the situation of the object in the VIC grid, AVG cannot. For the  $E$  fields parallel to the interfaces, not reported here, which are continuous, both VIC and AVG yield correct results.

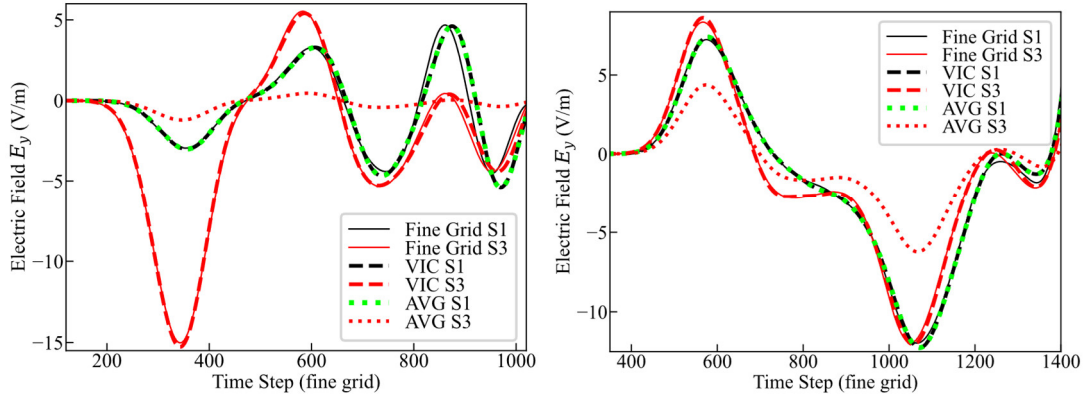


**Fig. 29.** Results for  $E_y$  at the outer interface In-1 (left part) and at the inner interface In-3 (right part). The outer interface In-1 is between vacuum and the medium of  $\epsilon_r = 50$  and the results of situation 1 are multiplied with 5. The inner interface In-3 is between media  $\epsilon_r = 5$  and  $\epsilon_r = 30$ , and the results of situation 1 are multiplied with 3.

Finally, we computed the average of the VIC and AVG errors on a  $66 \times 66 \times 66$  VIC cells cube composed of the  $60 \times 60 \times 60$  object surrounded with a layer of vacuum 3 cells in thickness. Note this volume includes all the nodes where the field is singular, at corners and edges. More precisely, we computed the average VIC or AVG error as

$$Err(it) = \frac{\sum_{m=1}^M |E_{VIC \text{ or } AVG}(it, m) - E_{fine}(it, m)|}{M} \quad (17)$$

where  $E_{VIC \text{ or } AVG}$  and  $E_{fine}$  are either  $E_x$ , or  $E_y$ , or  $E_z$ , at node  $m$ . The total number of  $E_z$  nodes,  $M$ , in a volume composed of  $N_i \times N_j \times N_k$  VIC cells can be calculated as  $(N_i + 1) \times (N_j + 1) \times N_k$ . Fig. 30 reports the VIC and AVG errors on the  $E_z$  component parallel to the incident  $E$  field. The incident wave was propagating in  $y$  direction, and we used the pulse (12) with a larger width ( $\tau = 269$  ps) to reduce the spurious effect of dispersion at late time. We can see that the VIC error is widely smaller than the AVG error, with a ratio of the order of 5 at the peak value. Similar reductions were observed on  $E_x$  and  $E_y$  components when using VIC instead of AVG.

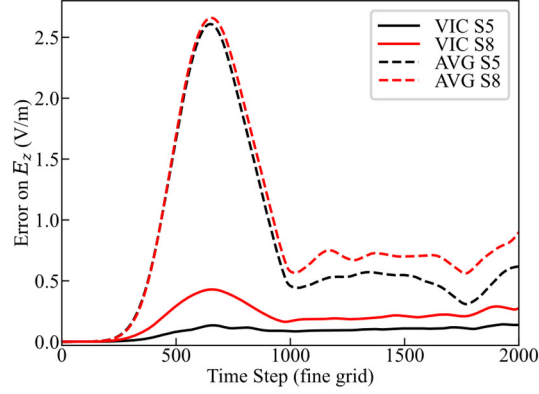


**Fig. 30.** The overall average error of the electric field  $E_z$  in situations 5 and 8 of the object (the largest errors of VIC). It includes all nodes in the object and 3 VIC cells of its surrounding vacuum.

## 6. Computational Requirements

Even with VIC cells only two times larger than the voxels, with dielectric voxels the update (9) can be used so that the number of VIC components to be stored and updated is 8 times smaller than with FDTD cells equal to the voxels size, and the number of time steps is two times smaller. From this, the memory requirements are about 8 time smaller with the VIC method. Concerning the CPU time, using (9) the loops of the updates of the  $E$  components are in the same form in the VIC grid and in the fine grid reference, so that the CPU time for processing one FDTD iteration of the VIC region (Fig. 4) can be reduced with a factor of 8 and thus the CPU time for a given physical time of simulation with a factor of 16. We observed even larger reductions, for example with the  $60 \times 60 \times 60$  VIC cells object in sub-section 5.4, using an i5 processor the time for processing the VIC region was reduced with a factor of 34. This was because the effectiveness of a processor decreases with the size of the problem, it was better with VIC than with the fine grid. For the whole domain including a Huygens surface and a 10-cell PML in both simulations (Fig. 4), whose computational costs are not proportional to the size of the VIC region, the ratio of CPU times was smaller, about 14.6. In conclusion to our experiments, with dielectric voxels the reduction of CPU time using the VIC method may depend on the computer and on the size of the problem to be solved, but, as expected, its actual value is at least of an order of magnitude.

With dispersive media in the voxels, where the  $D$  field must be computed in each voxel and the  $E$  field in each slice, the reduction of the CPU time could be significantly smaller if all the voxels of the VIC cells were different. However, in such realistic object as Human Body phantoms, many VIC cells are filled with identical voxels and only a few cells filled with more than three different media, so that large reductions of CPU time can also be achieved, will be illustrated in [13].

## 7. Conclusion

A simple method to account for non-homogeneous FDTD cells composed with voxels, denoted as VIC, has been introduced and tested with dielectric media on canonical 2D and 3D problems. The method can be extended to such dispersive media as Debye media [13].

Numerical experiments have been mainly performed with VIC cells two times larger than the voxels, i.e. with eight voxels in the VIC cells. Comparisons of the VIC method with a reference solution computed with a fine grid, with a cell equal in size to the voxels size, have shown that the VIC method is accurate at most nodes of the computational domain. A significant inaccuracy is only present at locations where the electric field is singular, nearby the corners and edges of dielectric objects [14]. This was expected, since an amount of error is always present nearby singularities with any FDTD calculation. Simply, with a VIC cell two times larger than that of the fine grid reference, the VIC error is larger. Ultimately, the observed VIC error is not specific to the VIC method, it is just inherent to the FDTD method.

Comparing with the AVG method that consists in averaging the permittivity's in the cells [15], VIC is by far more accurate. Especially at interfaces between media, where the electric field is not singular, VIC is accurate while with AVG the normal electric component is strongly erroneous. This is because AVG does not account for the discontinuity of the normal component at interfaces between voxels, while VIC does. In total, in a complex object like the one in Section 5.4, the number of nodes where the results are inaccurate is widely reduced with VIC, and at the remaining nodes the error is smaller, only due to the singularity of the field at corners and edges.

In applications of the FDTD method where the objects are given as sets of voxels, the VIC method allows the computational burden to be reduced in comparison with calculations with a cell equal in size to the voxels size. This is the case with dielectric objects, as in the experiments reported in this paper where reductions of CPU times larger than one order of magnitude can be achieved with VIC cells only two times larger than the voxels. In the field of bio electromagnetics where the phantoms are sets of voxels, the reduction will be smaller [13] due to the solution of an auxiliary equation in the voxels, but since many VIC cells are homogeneous, without interface between media [13], a large reduction of the overall CPU time will be also possible.

The principal drawback of the method is obviously the larger space and time steps. With VIC cells two times larger than the voxels, the upper bound of the frequency band is reduced by a factor of 2, which may be a limitation in some applications. Using a ratio of the VIC cell size to the voxels size larger than 2 is possible. This increases the drawbacks - inaccuracy at singular nodes, limitation of the bandwidth - and the advantages - reduction of the computational burden -. It may be of interest in some applications, depending on the balance between drawbacks and advantages.

Extension of the VIC method to lossy media is straightforward, and its extension to Debye media will be reported in [13]. Other applications can be envisaged, as using VIC as a subgrid method to incorporate subcell objects modeled with voxels in the FDTD cells, which is not possible with [8]-[12], or modeling staircased plane or curved interfaces within the cells. One or several VIC parts can be easily placed in the normal FDTD grid since there is no problem of connection as long as the boundaries between the different parts are in homogeneous regions. And inversely to many subgridding techniques, the VIC method does not suffer from instability, the stability condition remains the CFL condition of the large VIC grid, which means that as fine as needed voxels can be used to model the subcell structures.

### Acknowledgement

This work was supported in part by EU Horizon 2020 Research and Innovation Programme under Marie Skłodowska-Curie Action under Grant 101066571.

### References

- [1] K.S. Yee, "Numerical solution of initial boundary value problems involving Maxwell's equations in isotropic media," *IEEE Trans. Ant. Propag.*, vol. 14, no. 3, pp. 302-307, 1966.
- [2] G. Maloney, and G.S. Smith, "The efficient modeling of thin material sheets in the finite-difference time-domain (FDTD) method", *IEEE Trans. Ant. Propag.*, vol. 40, pp. 323-330, 1992.
- [3] R.J. Luebbers and K. Kunz, "FDTD modeling of thin impedance sheets", *IEEE Trans. Ant. Propag.* vol. 40, pp. 349-351, 1992.
- [4] K. Tekbas, F. Costen, J.-P. Bérenger, R. Himeno, and H. Yokota, "Subcell modeling of frequency-dependent thin layers in the FDTD method," *IEEE Trans. Ant. Propag.*, vol. 65, no. 1, pp. 278-286, 2017.
- [5] A. Alkandari, J.-P. Bérenger, R. Himeno, H. Yokota, and F. Costen, "Maloney and Smith Method for Modeling Debye-Media Thin Sheets in the FDTD Grid", *IEEE Trans. Ant. Propag.*, vol. 69, no. 4, pp. 2209-2217, 2021.
- [6] J. G. Maloney and G.S. Smith, "A comparison of methods for modeling electrically thin dielectric and conducting sheets in the finite-difference time-domain (FDTD) method", *IEEE Trans. Ant. Propag.*, vol. 41, pp. 690-694, 1993.
- [7] J.-P. Bérenger and F. Costen, "Theoretical Comparison of Methods for Modeling Thin Dielectric or Conducting Sheets in the FDTD Grid", *IEEE Trans. Ant. Propag.*, vol. 67, pp. 601-605, 2019.
- [8] N. Kaneda, B. Houshmand, and T. Itoh, "FDTD Analysis of Dielectric Resonators with Curved Surfaces", *IEEE Trans. Micr. Th. Tech.* vol. 47, pp.1645-1649, 1997.
- [9] A. Farjadpour, D. Roundy, A. Rodriguez, M. Ibanescu, P. Bermel, J. Joannopoulos, S. Johnson, and G. Burr, "Improving accuracy by subpixel smoothing in the finite-difference time domain", *Opt. Lett.*, vol. 31, pp. 2972-2974, 2006.
- [10] A. F. Oskooi, C. Kottke, and S. G. Johnson, "Accurate finite difference time-domain simulation of anisotropic media by subpixel smoothing," *Optics Letters*, vol. 34, pp. 2778-2780, 2009.
- [11] J. Liu, M. Brio, and J. V. Moloney "Subpixel smoothing finite-difference time-domain method for material interface between dielectric and dispersive media", *Opt. Lett.* 37(22) 4802-4804, 2012.
- [12] J. Hamm, F. Renn, and O. Hess "Dispersive Media Subcell Averaging in the FDTD Method Using Corrective Surface Currents", *IEEE Trans. Ant. Propag.* vol. 62, pp. 832-838, 2014.
- [13] K. Tekbas and J.-P. Bérenger, "FDTD Voxel-in-Cell method with Debye media", to be submitted.
- [14] J. Bladel, *Electromagnetic Fields*, Second Edition, Wiley, 2007
- [15] Dey and R. Mittra, "A conformal finite-difference time-domain technique for modeling cylindrical dielectric resonators", *IEEE Trans. Micr. Th. Tech.* vol. 45, pp.55-66, 1999.